Mechanistic Insights into Nitrile and Alkyne Covalent Inhibitors of the SARS-CoV-2 Main Protease

Ashim Nandi,[1] Mojgan Asadi,[1,2] Aoxuan Zhang,[1] Zhen T. Chu[1] and Arieh Warshel[1,*]

[1]Department of Chemistry, University of Southern California, Los Angeles, California 90089-1062, United States

[2]Department of Chemistry, Stanford University, Stanford, California 94305-5012, United States

*Correspondence: warshel@usc.edu

KEYWORDS: SARS-CoV-2, Inhibitors, Binding Energy. Kinetics, and QM/MM.

Abstract

The treatment of SARS-CoV-2 can be accomplished by an effective suppression of its 3CL protease (3CL^{pro}), also known as the main protease (M^{pro}) and nonstructural protein 5 (nsp5). Covalent inhibitors can irreversibly and selectively disable the protease, particularly when they are highly exothermic. Herein we investigated the distinct kinetic behaviors exhibited by two covalently linked SARS-CoV-2 inhibitors. One of these inhibitors features a nitrile reactive group, while the other has this group replaced by an alkyne group, a less reactive electrophile. Our investigations involve the assessment of the free energy surfaces of the key feasible mechanisms that is direct and water-assisted involve in the rate-determining proton-transfer nucleophilic attack step through the utilization of both ab initio and empirical valence bond (EVB) simulations. The calculated free energy profiles show that substituting the nitrile group with alkyne increase the chemical barrier but leads to very exothermic reaction energy and is an irreversible process as opposed to nitrile, which is moderately exothermic and reversible. We also examine the time-dependence of IC50 inhibition by applying a novel kinetic simulation approach, which is particularly important in studies of covalent inhibitors with a very exothermic bonding step. Our computational approach gave a good agreement between the calculated and observed values of the time dependance results for the nitrile and alkyne inhibitors.

Introduction

The coronavirus disease 2019 (COVID-19), caused by the severe acute respiratory syndrome coronavirus 2 (SARS-CoV-2), has been one of the most devastating pandemics of recent times. There has been significant effort to develop antiviral therapeutics targeting two proteases of SARS-CoV-2: the main protease (M[pro]) and papain-like protease (PL[pro]).[1–3] Out of these targets, M[pro], also known as 3-chymotrypsin-like protease (3CL[pro]), has received significant attention in the development of antivirals, i.e., protease inhibitors, to combat COVID-19,[4–7] with the fundamental aim to disrupt the function and life cycle of SARS-CoV-2.[8] Several small-molecule inhibitors of SARS-CoV-2 M[pro] have been discovered, with a few progressing into early-phase human clinical trials.[9,10] Covalent enzyme inhibitors are of significant interest as biochemical tools and therapeutic drugs.[11] Previous authors have summarized the distinctive advantages and disadvantages of covalent enzyme inhibition in drug and inhibitor design.[12–14] As the treatment of COVID-19 requires disabling the activity of M[pro], covalent inhibitors with high exothermicity and irreversible binding to M[pro] can be important candidates for antiviral treatments. A notable therapeutic strategy for COVID-19 is to design inhibitors with an electrophilic reactive group ("warhead") that binds to the nucleophilic target cysteine 145 (Cys145) in M[pro]. Cys145 is essential for the catalytic activity of M[pro], so blockage or modification of this residue is detrimental to the virus.[15–19] Nirmatrelvir is a new FDA-approved medication developed for the treatment of COVID-19[20] that has a nitrile warhead and binds covalently and reversibly to Cys145 . There are several known derivatives of nirmatrelvir[21], some of which are reversible, while others lead to irreversible catalytic reactions.

Recently, Zhang and co-workers have demonstrated the effectiveness of latent electrophilic warheads,[22] such as terminal alkynes in inhibiting M[pro] compared to more reactive electrophiles like acrylamides. These terminal alkyne warheads demonstrate marked specificity for M[pro] due to their lack of intrinsic reactivity, which circumvents nonspecific binding to other cellular proteins. Upon activation within the active site of M[pro], these warheads have shown potent inhibition, as confirmed through biochemical assays and structural analysis via X-ray crystallography. Notably, these terminal alkyne-based inhibitors have also exhibited promising antiviral activity in cellular models of COVID-19, indicating their potential as effective therapeutic agents. [23,24]

Our prior computational investigations into covalent inhibitors targeting M[pro] explored the mechanism of α-ketoamide inhibitors[19] and the estimation of their absolute binding free energies[19]. This study has been arguably the first calculation of the actual binding energetics of covalent inhibitor of M[pro]. Our subsequent study introduced a more effective thermodynamic cycle for evaluating absolute binding energies.[25] The present study centers on a comparative analysis between nirmatrelvir and its alkyne-substituted counterpart, where the nitrile group is substituted with an alkyne group[23,26] (see Figure 1). It is important to note that previous QM/MM studies[27–31] have not focused on or thoroughly investigated the actual binding energetics of inhibitors targeting the SARS-CoV-2 M[pro].

Our objective is to elucidate the underlying factors behind the distinct behaviors exhibited by these inhibitors, particularly with regard to the time-dependent inhibition process. To achieve this goal, we conducted a comprehensive exploration of the reaction mechanisms associated with each inhibitor through ab initio and empirical valence bond (EVB) simulations. A prior experimental study[22] has shown that the alkyne derivative inhibits M[pro] approximately five times more effectively than nirmatrelvir, with an IC50 value of ~0.76 μM for nirmatrelvir and IC50 ≥ 0.063 μM for the alkyne derivative, following a preincubation period of three hours.[23,32] Our simulations have not only substantiated the exothermic nature of the alkyne substitution but also replicated the corresponding time-dependent IC50 trend, corroborating the assertion that the alkyne derivative is a more potent inhibitor compared to nirmatrelvir.
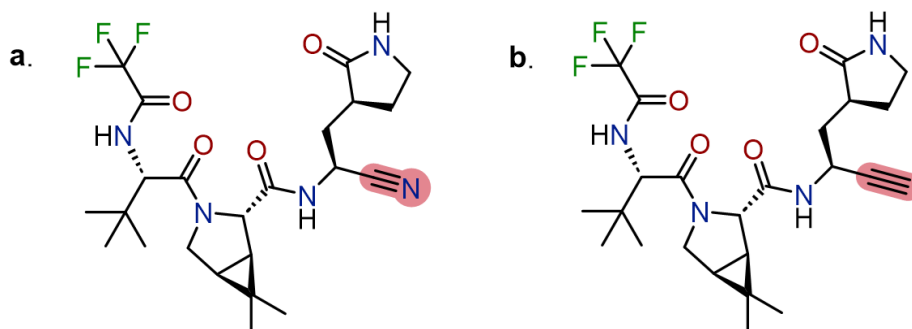

Figure 1. Chemical structure of nirmatrelvir showing (a) nitrile and its (b) alkyne derivative warhead. The warhead is highlighted.

Computational Methods

System Equilibration

Our study began with the utilization of a co-crystal structure of the main protease (M^{pro}) of SARS-CoV-2 and the drug nirmatrelvir. The specific structure employed was sourced from the Protein Data Bank (PDB), under the identifier 7RFS.[32] In this structure, nirmatrelvir is observed to be covalently bonded to the cysteine residue at position 145 (Cys145) of the protease. To investigate the effects of an alkyne derivative, we referenced a similar co-crystal structure wherein the derivative forms a covalent bond at the same cysteine residue, as detailed in the study by Zhang et al. (PDB 8FY6).[22] Following the selection of the initial structures, we performed molecular dynamics simulations using the GROMACS software suite (version 2021)[33] with 40 ns trajectories. The Amber force field (ff14sb) was employed to model the interactions within the system. Subsequently, we carefully selected suitable initial configurations from the simulation trajectories to serve as starting points for the subsequent calculations involving the empirical valence bond (EVB) method. In order to define the force field parameters for the ligand atoms, we referred to the generalized Amber force field (GAFF) using AmberTools 21.[34]

ab initio Calculations

The reaction mechanisms pertinent to the aqueous phase, crucial for the calibration of EVB study (see below) were explored using ab initio computational methods. The study entailed modifying the inhibitor molecules under consideration by truncating their reactive groups and capping the resulting sites with a methane moiety, as depicted in Figures S1 and S2 in the Supplementary Information section. For the computational analysis, we employed the Gaussian 16 software package.[35] The quantum mechanical calculations were carried out using Density Functional Theory (DFT), specifically applying the B3LYP functional combined with the 6-311+G(d,p) basis set.[36] The choice of this method is supported by recent studies[27] showing that B3LYP accurately describes the proton transfer and nucleophilic attack of a thiolate on a Michael acceptor. Additionally, in an *ab initio* benchmark study[37] on the proton transfer between CYS145 and HIS41 in SARS-CoV-2 M^{pro}, B3LYP demonstrated superior performance when benchmark against high-level LCCSD(T) methods and experimental data. The GD3BJ correction was applied to account for dispersion interactions, and solvent effects were modeled using the SMD method.[38] Both the

geometry optimizations and energy evaluation were conducted under this theoretical framework. The SCF convergence criteria were set by using the keyword "opt = tight", which sets the maximum and root-mean-square (RMS) forces to 1.5×10^{-5} and 1.0×10^{-5} hartree/bohr and the maximum and RMS displacements to 6.0×10^{-5} and 4.0×10^{-5} bohr. The "ultrafine" grid, which is a pruned direct product of a 99-point Euler−MacLaurin radial grid combined with a 590-point Lebedev angular grid was employed for all DFT calculations. Intrinsic reaction coordinate (IRC) calculations were conducted to confirm that the transition state smoothly connects to both the reactant and product sides.

EVB Simulations

The EVB methodology utilizes a hybrid quantum mechanics/molecular mechanics (QM/MM) framework to model chemical reactions through a combination of relevant diabatic states. This enables an efficient exploration of reaction processes,[39,40] as detailed in the Supplementary Information. Prior studies have validated the utility of EVB in analyzing protease inhibition thermodynamics.[19,41–44]

Our EVB calculations were executed with the Q6 simulation software package.[45] Within these simulations, the active site of the reaction comprises the inhibitor's reactive groups, Cys145, His41, and a catalytic water molecule in nitrile and is designated as region 1. The remainder of the enzyme-solvent system was categorized as region 2. Electrostatic potential (ESP) charges for atoms in region 1 were derived from Gaussian 16 calculations,[35] which were then transformed into Restrained Electrostatic Potential (RESP) charges using the Antechamber tool from AmberTools 21.[34] The initial position of the sulfur in cysteine was used to set the center of the simulations sphere. The system was immersed in a water sphere with a diameter of 25 Å, where the water molecules were described by the TIP3P model[46] and subjected to the SCAAS boundary conditions,[47] where the long-range effects were treated by the local reaction field.[48]

The multi-stage optimization of each reaction step commenced with a local energy minimization, constraining all heavy atoms with a force constant of 20 kcal/ (mol Å^2), followed by a gradual relaxation of these restraints and a temperature increase from 5 to 300 K over 1 ns for system equilibration. Subsequent to this, free-energy perturbation/umbrella sampling (FEP/US)[49]
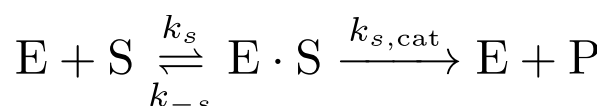
simulations were conducted on the equilibrated systems to obtain the free-energy profiles. Ab initio activation and reaction energy data from reference solution reactions were then employed to fine-tune the EVB Hamiltonian for each step of the reaction mechanism. For comprehensive sampling, we performed five umbrella sampling replicas, each comprising 100 frames with a 5 ps duration per frame to ensure statistical reliability and robustness of the results. Additionally, we also repeated FEP sampling using from protein structures from various equilibration times (200 ps to 2 ns) for concerted proton transfer-nucleophilic attack reactions and found no substantial change in the predicted free energies.
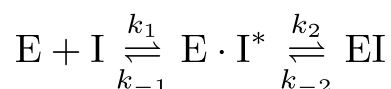
PDLD/S-LRA-2000 method

The non-covalent binding free energy of the inhibitor to M^{pro} was calculated by the Protein Dipoles Langevin Dipoles method in its linear response approximation (PDLD/S-LRA-2000) using a sampling of 4 different configurations collected at every 20 ps of successive MD relaxation.[50–53] This method, implemented in the MOLARIS-XG package,[54] efficiently computes binding energies by constructing proper thermodynamic cycles, as detailed in our previous work.[55,56] The PDLD approach represents water molecules semi-macroscopically as Langevin dipoles. The energy is evaluated using the linear response approximation,[55] which averages the charged and uncharged states. The entire system is embedded within a 20 Å simulation sphere centered around the Nirmatrelvir inhibitor and surrounded by a bulk continuum. The electrostatic energy was scaled using a dielectric constant of $\varepsilon = 4$ for the protein,[57,58] and the non-electrostatic term, which is not specific and may vary by system, was scaled by a factor of 0.75 and is detailed in Ref[53].

Time-dependent kinetic simulations

In the case of very exothermic covalent inhibitors, the justification of the use of the standard kinetic assay equations is far from obvious. Thus we used a kinetic simulation to evaluate the time dependence of the competitive inhibition of M^{pro} in the experimental assay conditions by solving the first-order system of equations as described in ref[41], with the exception that the inhibitor may be reversible. That is, competitive inhibition is described by the scheme,

$$\mathrm{E} + \mathrm{S} \underset{k_{-s}}{\overset{k_s}{\rightleftharpoons}} \mathrm{E} \cdot \mathrm{S} \xrightarrow{k_{s,\mathrm{cat}}} \mathrm{E} + \mathrm{P}$$

$$\mathrm{E} + \mathrm{I} \underset{k_{-1}}{\overset{k_1}{\rightleftharpoons}} \mathrm{E} \cdot \mathrm{I}^* \underset{k_{-2}}{\overset{k_2}{\rightleftharpoons}} \mathrm{EI}$$

where E is the enzyme, S is the substrate, P is the product, I and I^* are the free and bound inhibitors, and EI is the covalently bound enzyme-inhibitor complex. The equilibrium constant $K_\mathrm{i} = k_{-\mathrm{s}}/k_\mathrm{s}$, and catalytic rate $k_{\mathrm{s,cat}}$ of the substrate are determined by experimental characterization of the enzyme. The equilibrium dissociation constant $K_i = k_{-1}/k_1$ is determined from the calculated PDLD/S-LRA-2000 binding affinity,[51] ΔG_{bind} by $K_i = e^{\Delta G_{\mathrm{bind}}/k_b T}$, while the rates k_2 and k_{-2} are determined from the barrier and reverse barrier, respectively, in the EVB profile using the Arrhenius relation. As the second step of the inhibition scheme is the covalent and possibly irreversible step, k_2 is equivalently denoted as k_{inact}.

Results and Discussion

The key residues of M$^{\mathrm{pro}}$ include Cys145, His41, His163, His172, Glu166, and Ser144 (Figure 2) in its active site, which together form the oxyanion hole for the covalent and non-covalent binding interactions. The catalytic dyad Cys145-His41, in which the Nε2 atom of His41 is 3.6Å away from the SG atom of Cys145, participates in the first proton transfer. We initially observed that the protonation state of His163 plays a crucial role in catalytic activity and binding affinity. One possible rationale is that the position of carbonyl oxygen in pyrrolidin-2-one of the inhibitors is stabilized by hydrogen bonding with His163. Thus, we proceeded with our calculations assuming Nε2 in His163 is protonated. We explored different ionizable states of His164 and His172 and overall, we found no significant changes in the EVB energy barrier when changing the protonated nitrogen from Nε2 to Nδ1 or to both.
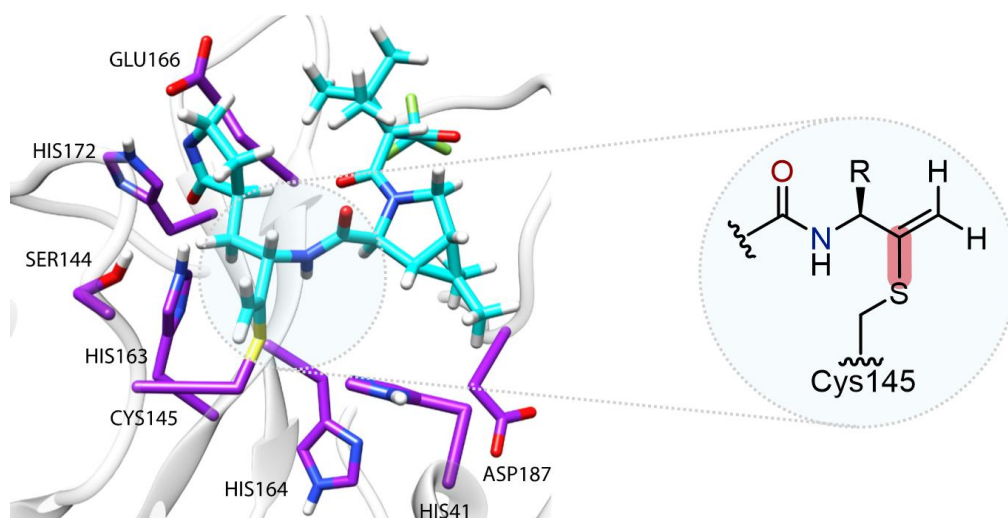
Figure 2. Structure of M^pro covalently bound with the alkyne derivative of nirmatrelvir (PDB 8FY6). The alkyne warhead covalently bonded to the Cys145 after the proton-transfer nucleophilic attack (PT-NA) is circled. Surrounding key residues for binding and catalytic activity are also shown. The binding poses and the conformers of the catalytic residue are essentially identical to the structure of M^pro covalently bound with nirmatrelvir (PDB 7RFS).

ab Initio Calculations

As a starting point, we explored potential reaction pathways for the covalent binding of nitrile and alkyne functional groups to cysteine in a solution phase. These pathways will serve as reference reactions for our subsequent EVB calculations in water. We delineated each reaction pathway into two primary steps: a proton transfer between a cysteine and a histidine residue, and a concerted mechanism involving a proton transfer coupled with a nucleophilic attack (PT-NA), which can occur directly or with solvent assistance as discussed below.
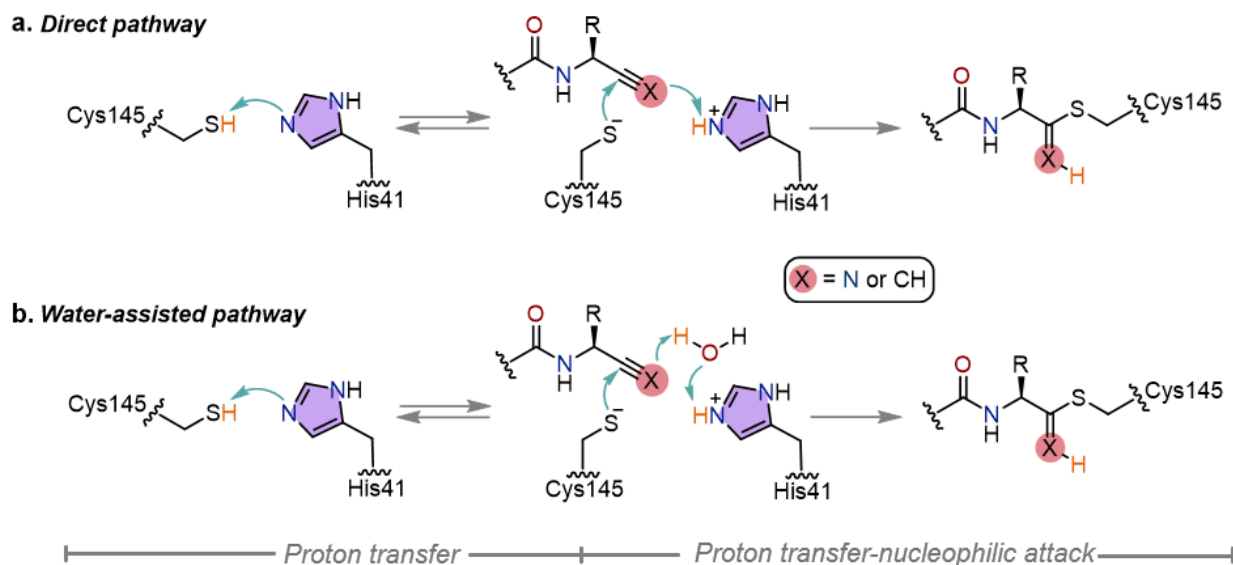
Figure 3. Reaction mechanisms for nirmatrelvir displaying (a) direct and (b) water-assisted pathways involving nitrile (X = N), and alkyne (X = CH) as warhead.

The reaction mechanism initiates by calculating the free energy of the first proton transfer (PT) process for both nirmatrelvir and its alkyne warhead. The PT between CYS145 and HIS41 for the reference solution reaction in the presence of inhibitor was taken from our previous work[59] where we report a $\Delta G_{\mathrm{PT,obs}}$ of 7.0 kcal/mol in water. We assumed that the different warheads of the inhibitors studied here and in the Ref[59] have a similar impact on the PT process. Following the formation of the ion-pair intermediate during the PT process, we explored the proton transfer-nucleophilic attack (PT-NA) step using DFT calculations.

For the direct PT-NA mechanism involving the nitrile, our calculations show a relative free energy barrier ($\Delta G^{\ddagger}$) of 22.4 kcal/mol and a reaction energy (ΔG_0) of -1.1 kcal/mol, indicating a slightly thermoneutral reaction. The free energy profile is displayed in Figure 4a. Additionally, a more accessible pathway is expected involving a water-assisted PT-NA, where water mediates the H-transfer from the nitrogen of histidine to oxygen. Our computational results show that the involvement of water lowers provides a similar barrier ($\Delta G^{\ddagger}$ of 18.1 kcal/mol) compared to the direct pathway, however the reaction becomes more exothermic (ΔG_0 = -5.0 kcal/mol). In summary, the reaction of both pathways is kinetically feasible; however, it is more thermodynamically favored in the presence of water. Recent QM/MM studies on SARS-CoV-2

M[pro] inhibition with nitrile derivatives also support that water-assisted PT-NA is the favorable path.[28,60] It is worth noting that previous QM/MM work[28] explored the direct PT-NA process but could not locate the TS, highlighting the challenges of this pathway. In our studied systems, we will explore both the direct and water-assisted PT-NA within the protein environment using EVB simulations (*vide infra*).

For the alkyne derivative, the free energy profile is shown in Figure 4b. In this case, the barrier for the water-assisted channel is found to be substantially lower by 13.4 kcal/mol compared to the direct path ($\Delta G^{\ddagger}$ of 22.9 versus 36.3 kcal/mol). However, the reaction energy is slightly more exothermic in the direct path by 0.7 kcal/mol as compared to water-assisted (ΔG_0 of -26.8 versus -27.5 kcal/mol). The overall free energy profile might appear to deviate from Hammond's postulate in the case of the alkyne, as well as for the same reaction in protein environment (*vide infra*), which states that more exothermic reactions should yield lower activation barriers. However, this postulate applies to elementary stepwise reactions, whereas our study involves a concerted pathway, so the kinetics can differ, as we have also reported in our earlier works involving concerted mechanism.[42,53]
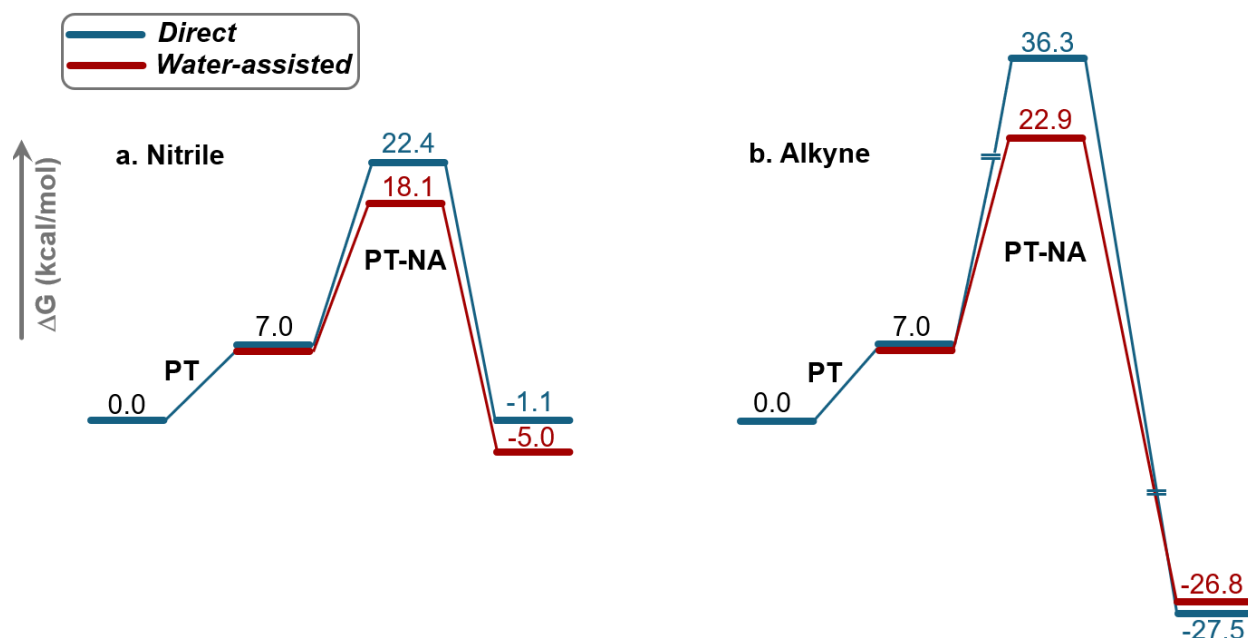

Figure 4. ab initio profile for the direct (in blue) and water-assisted PT-NA (in red) reaction mechanism of nirmatrelvir with (a) nitrile and (b) for the alkene derivative as warhead.

Additionally, we also explored alternate plausible mechanism involving the role of Asp187 in stabilizing the TS. This mechanism, however, was found to be very endothermic and thus inconsistent with the proposed Cys145-His41-Asp187 catalytic triad hypothesis.[61]

The calibration of the EVB simulations was determined by the above mechanistic explorations, as discussed in detailed below.

EVB Calculations

As detailed above, the ab initio calibrated EVB Hamiltonian for the reaction in solution provides the basis for modeling the corresponding enzymatic reactions. The calibrated EVB parameters as well as a summary of the reaction routes that were explored by EVB simulation are given in the Supporting Information. The free energy profile for the rate-determining state[62] in the studied mechanism i.e., the PT-NA step was evaluated in a reverse order using the EVB, starting from the available corresponding structures for the covalent form of the ligand. However, for the first PT process, we estimated ΔG_{PT} using the PDLD/S-LRA-2000 method, applying the thermodynamic cycle shown in Fig. 5, similar to the strategy used in our previous work.[25] In this approach, we calculated the binding free energy of the ion-pair intermediate in the protein (see upper panel of Fig. 5) with CYS145, HIS41, and the inhibitor treated as the QM region. To the ΔG_{QM}^{P} obtained from the upper panel, we added the ΔG_{exp}^{w} from the reference solution reaction (lower panel), which is +7.0 kcal/mol, as mentioned above. This resulted in ΔG_{PT} of 4.0 for the nitrile and 8.2 kcal/mol for the alkyne (see Table S1 in for SI for details).
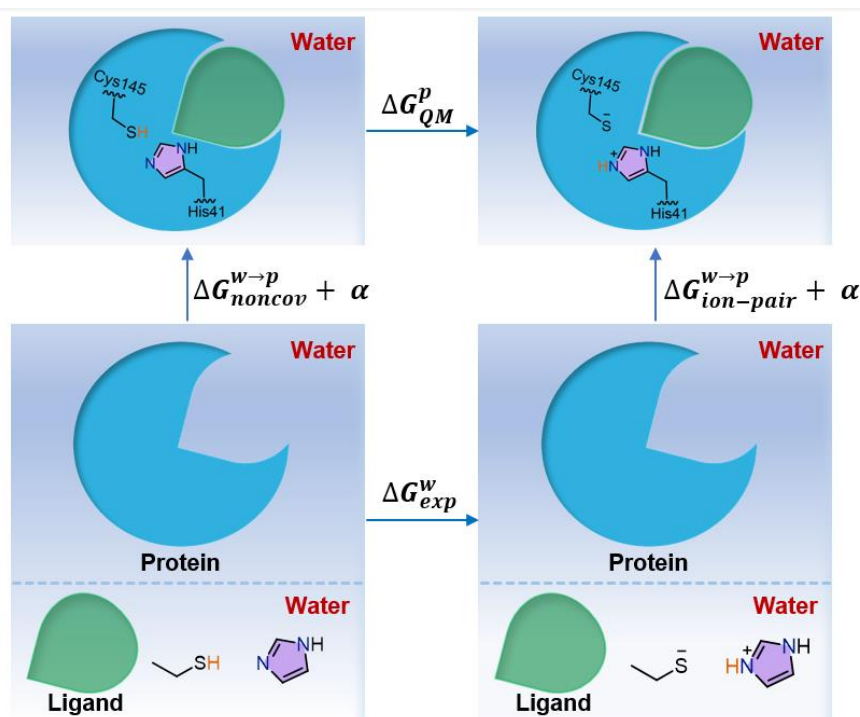
Figure 5. Thermodynamic cycle for calculating the absolute binding free energy of the inhibitor before and after the proton transfer (PT) process. α is the bond energy which is canceled out in the cycle.

Next, we turned our attention to the PT-NA step. Figure 6 present the EVB free energy profile for our reference solution reaction and in protein for nirmatrelvir (nitrile), comparing the direct (in blue) and water-assisted (in orange) mechanisms. Our calculations show that the rate-determining transition state (TS) is stabilized in the protein for both reaction mechanism giving $\Delta G^{\ddagger}$ of 22.4 kcal/mol versus 16.9 kcal/mol when transitioning from water to protein for the direct mechanism, whereas, for the water-assisted path it is $\Delta G^{\ddagger}$ of 18.1 kcal/mol versus 13.2 kcal/mol. This indicates that the water-assisted channel is the favorable pathway, this result is in agreement with other QM/MM studies,[60] which predicted a $\Delta G^{\ddagger}$ of 16.3 kcal/mol for the water-assisted mechanism.

Regarding the reaction free energy, although our calculation shows that the nirmatrelvir (nitrile) overall reaction energy in both direct and water-assisted is slightly exothermic (see Figure 6). It is crucial to mentioned that the free energy profile presented in Figure 6 does not include the absolute

binding free energy of the non-covalent complex, which is crucial and have an significance influence on the reaction energies, which we studied using PDLD/S-LRA-2000 (*vide infra*).
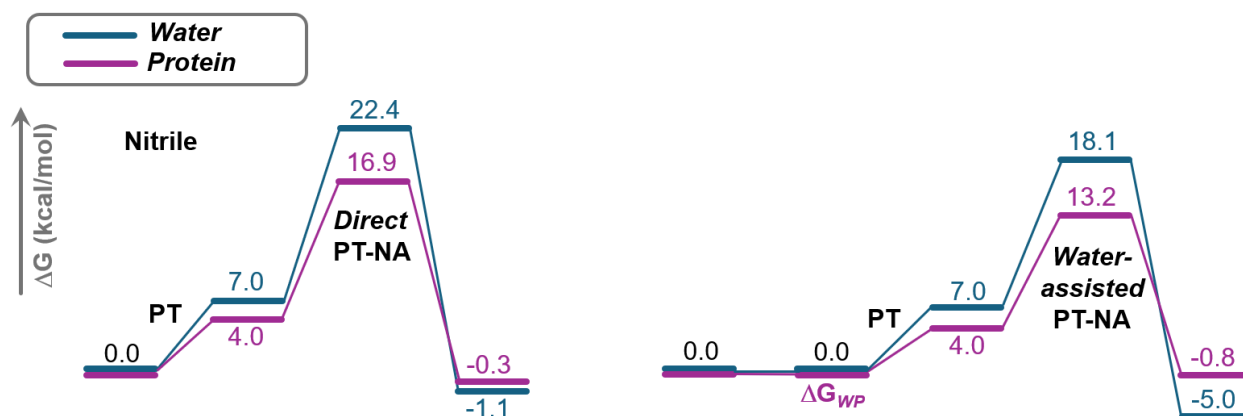

Figure 6. EVB profiles for the reaction mechanism of nirmatrelvir (nitrile) in water and protein for the (a) direct and (b) water-assisted PT-NA path. The direct and water assisted mechanisms are depicted, respectively, on the left and right sides of the figure.

For the alkyne derivative, our calculations for the rate-determining state in the water-assisted pathway show a lower barrier than the direct (see Fig. 8) in protein, similar to the nitrile case. However, for the alkyne derivative, the water-assisted PT-NA free energy profile must account for the energetics of moving a water molecule from the bulk to a catalytic position, as there is no pre-existing water molecule in this position in the crystal structure, unlike in the nitrile case. Usually, this energy is very small but here we examined this factor in view of the difference between the nitrile and alkyne. The examination should have been done in principle, by evaluating the PMF for water penetration by umbrella sampling or by our water flooding approach.[63] However, since we are dealing with a relatively small effect, we used a simplified alternative by evaluating the RDF for the nitrile and the alkyne, converting the RDF to PMF (which is presented on Figure 8) and then took the deference between the two PMFs as the energy of water penetration in the alkyne case. Since in the case of the nitrile we already have a water molecule in the catalytic position, by this procedure we estimate the water penetration penalty to be less than 1 kcal/mol.
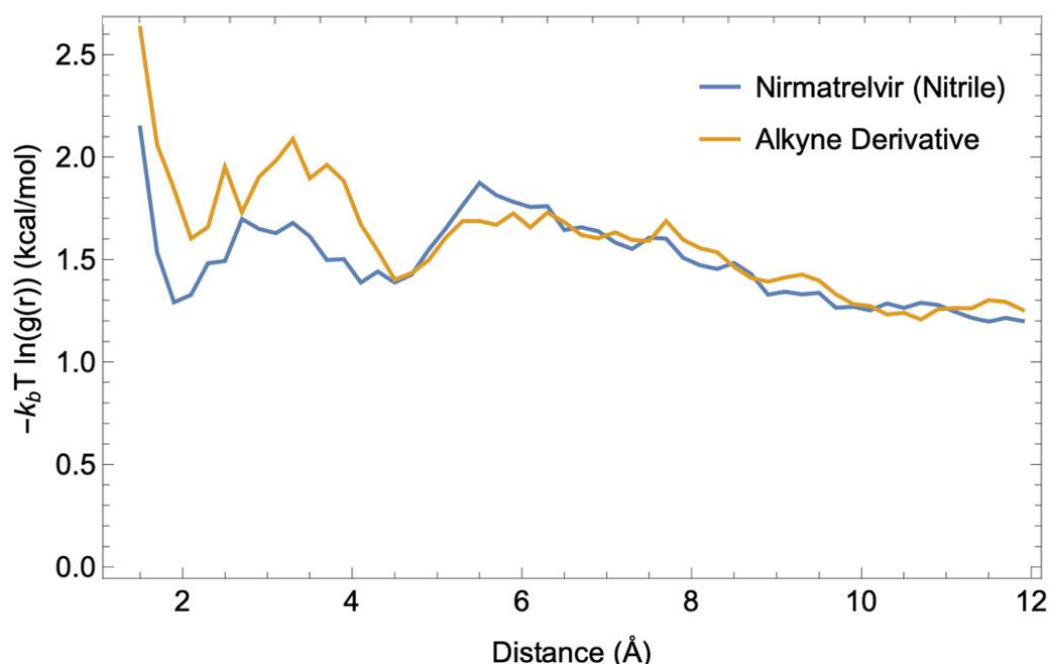
Figure 7. Potential of mean force (PMF) of water penetration into the active site. The PMF is evaluated from the radial distribution function (RDF) g(r), where r is the distance between the oxygen atom of a water molecule and the estimated position that enables a water-assisted PTNA, defined as the geometric center of the inhibitor's electrophile carbon, the inhibitor's carbonyl oxygen, and Nε2 in histidine.

Incorporating this water penetration (ΔG_{WP}) energy, the overall EVB barriers for the direct and water-assisted pathways in the PT-NA are 28.3 kcal/mol and 22.4 kcal/mol, respectively, corresponding to slow inactivation rates $\boldsymbol{k_{\text{inact}}}$ of 1.6 x 10^{-8} s^{-1} and 1.5 x 10^{-3} s^{-1}. These results suggest that the direct mechanism is impossible to occur under normal experimental conditions, while the water-assisted pathway is the favorable route. Additionally, the reaction energies, excluding non-covalent inhibitor binding, are highly exothermic and irreversible for both mechanisms, with substantial reaction free energies of -34.3 kcal/mol for the direct pathway and -20.6 kcal/mol for the water-assisted pathway.
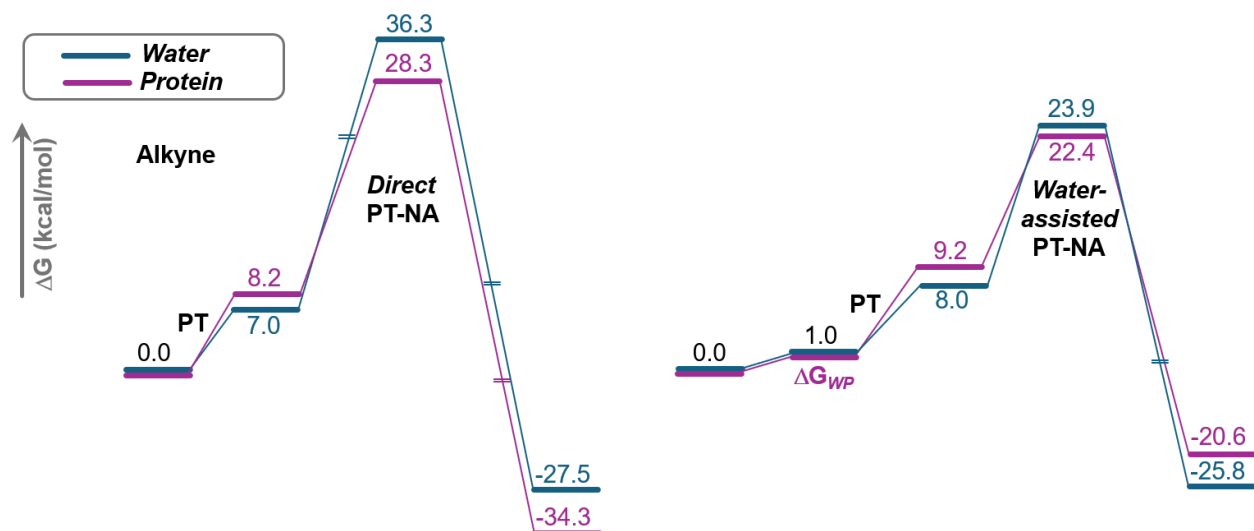
Figure 8. EVB profiles for the reaction mechanism of the nirmatrelvir alkyne derivative for the (a) direct (b) water assisted mechanisms are depicted. The water-assisted PT-NA profile includes a water penetration (WP) contribution of 1 kcal/mol (described below).

As a final step, we investigated the crucial non-covalent binding process of the inhibitors and incorporated the non-covalent binding energy (ΔG_{bind}) into the EVB reaction profile. Our PDLD/S-LRA-2000 calculations yield ΔG_{bind} values of -9.8 kcal/mol for the nitrile and -11.2 kcal/mol for the alkyne. Incorporating these values into the EVB profile for the protein, as shown in Figures 6 and 7, results in the complete free energy profile depicted in Figure 9.
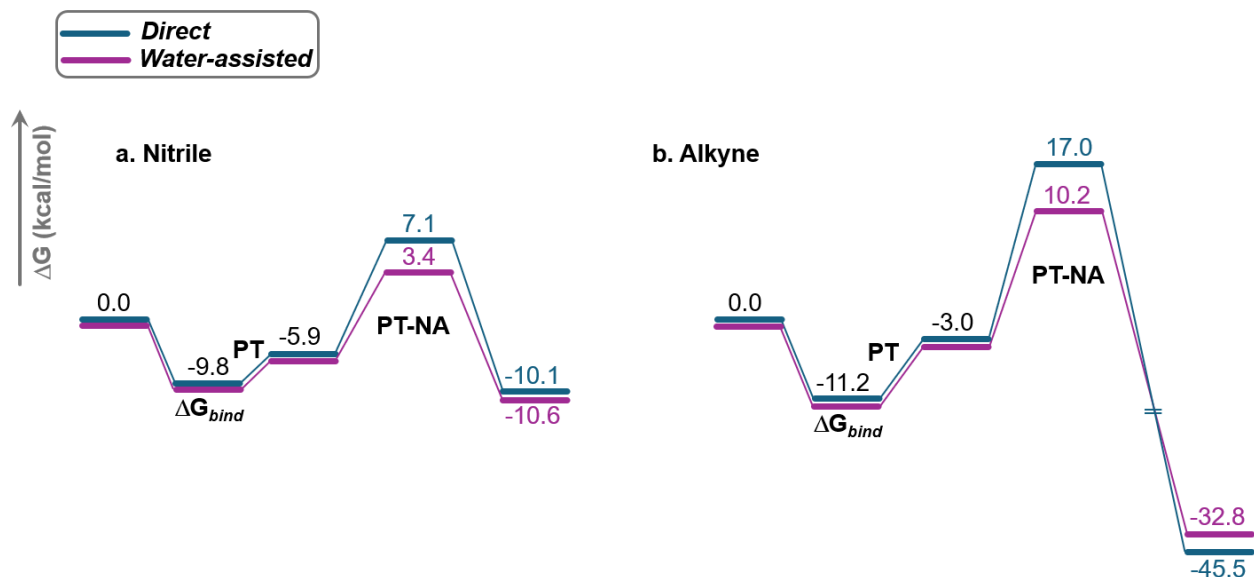
Figure 9. Inclusion of the PDLD binding to the EVB profile for the direct and water-assisted reaction mechanisms of; (a) nitrile and (b) alkyne derivative in protein environment.

In both the direct and water-assisted mechanisms, it is observed that ΔG_{bind} is an important intermediate that leads to a reduction in the overall reaction energies. After incorporating ΔG_{bind} into the reaction profile, the reaction energy becomes -10.1 and -10.6 kcal/mol for the direct and water-assisted path. Other QM/MM studies have reported exothermicity values of -8.8 kcal/mol[17] and -9.5 kcal/mol[60] for the water-assisted mechanism, consistent with our results.

For the alkyne derivative, the overall reaction energies are -45.5 kcal/mol for the direct pathway and -32.8 kcal/mol for the water-assisted pathway. We do not have experimental data to validate our predictions. However, our calculated barriers of 22.4 kcal/mol for the kinetically feasible water-assisted path is in excellent agreement with similar alkyne derivative inhibitors of Cathepsin K studied in a recent QM/MM study.[64] This study reported a barrier of 20.1 kcal/mol for the direct mechanism, where the experimental barrier is 22.5 kcal/mol,[65] in excellent agreement with our water-assisted mechanism.

At this point, we would like to highlight the stark contrast between the EVB profile for the nitrile and alkyne. The lower activation barrier for the nitrile compared to the alkyne can be attributed to the better stabilization of the transition state due to its polar warhead during the PT-NA process. On the other hand, the low exothermicity of the nitrile and the high exothermicity of the alkyne (see Fig. 8) may be attributed to the fact that the alkene-based complex forms a more stable and stronger covalent bond than the imines after the PT-NA process. This trend in our reaction energy is consistent with other QM/MM studies on similar inhibitors. [64]

Kinetics Simulation of Inhibitor Selectivity

To address the task of linking the estimated and observed kinetics, we employed a simulation approach similar to the one we previously developed for studying the irreversible inhibition of tyrosine kinases.[41] Typically, IC50 and K_i are correlated in cases of reversible inhibitor binding. However, in this study, we are dealing with two distinct reactions: one is highly exothermic and irreversible, while the other is moderately exothermic and reversible. Consequently, it is essential

to use the calculated reaction free-energy profiles and kinetic simulations to replicate the experimental observable, specifically the time-dependent IC50(t). This should be done in conjunction with comparing the effective rate constant, $k_{\text{eff}} = k_{\text{inact}}/K_i$, as indicated by the binding energies and reaction rates.

We used a simple competitive inhibition scheme to generate the trend of the experimentally observed kinetics. The inhibition assay was simulated, subjecting the enzyme to pre-incubation with the inhibitor for a certain amount of time, and then calculating the initial velocity of product formation upon adding the substrate to the assay. We used the same initial conditions as the assay used by Zhang and co-workers[22] ($[S]_0 = 20\ \mu M$ and $[E]_0 = 0.5\ \mu M$) for both inhibitors. Additional simulation details and assay-dependent parameters are listed in the Supplementary Information. Table 1 lists the calculated kinetic and thermodynamic parameter along with simulated and experimental IC50 values for the direct and water-assisted mechanism. The simulated IC50 for the nitrile inhibitor does not change significantly between the two mechanisms, which is an indication of a reversible inhibition process. However, for the alkyne, the IC50 values change significantly with pre-incubation time. These results are consistent with experimental findings.[22]

Table 1: Summary of calculated energetics and simulated IC50 values for the water-assisted mechanism, compared with experimental IC50 values for the nitrile and alkyne derivative.[22] Energies are in kcal/mol while IC50 values are in μM.

Inhibitor	Mechanism	EVB		PDLD	Simulated IC50			Experimental IC50		
		$\Delta G^{\ddagger}$	ΔG_0	ΔG_{bind}	30s	15min	3h	0h	15min	3h
Nitrile	Direct	16.9	-10.1	-9.8	1.12	0.58	0.57	0.34 ± 0.11	0.56 ± 0.32	0.76 ± 0.27
	Wat-assist.	13.2	-10.6		1.02	0.43	0.43			
Alkyne	Direct	28.3	-45.5	-11.2	15.28	0.94	0.28	15.72 ± 7.29	0.30 ± 0.12	0.063 ± 0.015
	Wat-assist.	22.4	-32.8		15.28	0.94	0.27			

The simulated time-dependent IC50 curves for the direct and water-assisted mechanisms for the nitrile and alkyne derivatives are shown in Figures 9 and 10. The irreversibility of the reaction with the alkyne warhead is evident from the strong dependence of IC50 on pre-incubation time, in

stark contrast to the nitrile case. The predicted IC50(t) of nirmatrelvir yield a value of 570 nM for the direct mechanism and 430 nM for the water-assisted pathway after 3 hours of pre-incubation. For the alkyne derivative, the IC50 is approximately 270 nM, indicating a two-fold greater potency, which agrees with the trend in the experimental assays reporting a ten-fold increase in potency.

While our simulated IC50 values (Table 1) are in close agreement with experimental data, they show little dependence on whether a direct or water-assisted mechanism is used for the nitrile warhead. However, for the alkyne derivative, the available experimental k_{eff} provides clear insight into which mechanism is favored. The experimental k_{eff} for the alkyne inhibitor is reported as 5.3×10^7 M^{-1}s^{-1}, while our calculated k_{eff} from EVB and binding affinity simulations is 0.29 M^{-1}s^{-1} for the direct mechanism and 2.3×10^4 M^{-1}s^{-1} for the water-assisted mechanism. The latter is in reasonable agreement with the observed value, further supporting our EVB results that the water-assisted mechanism is the favored pathway.
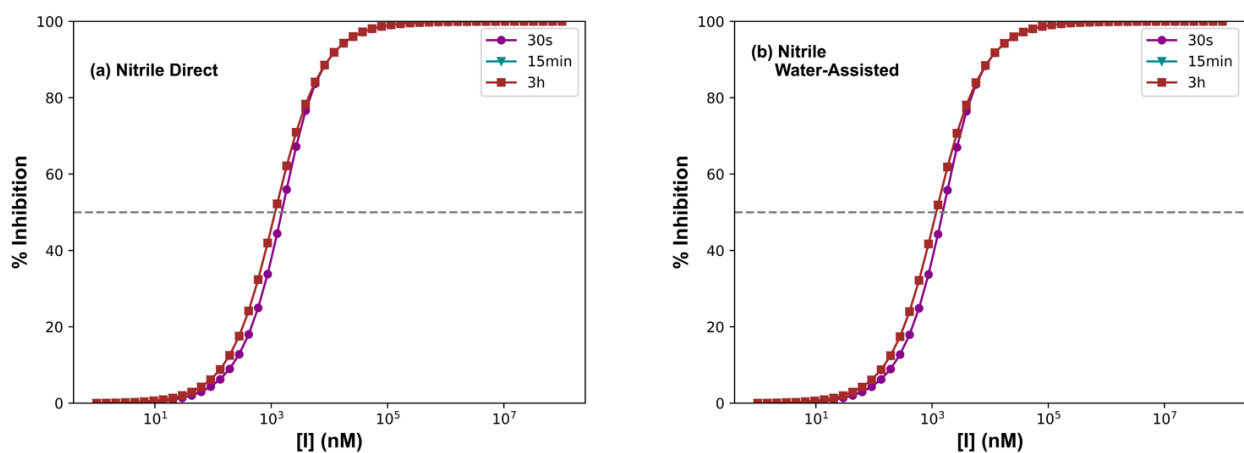

Figure 9. Simulated incubation assay of M^{pro} under different preincubation times in varying concentrations of Nirmatrelvir, using the predicted EVB reaction kinetics of both (a) the direct and (b) water-assisted mechanism. The IC50 is obtained as the inhibitor concentration for which the velocity of product formation is cut by 50% (dashed line). Note, the green (15 min) curves overlap with the red (3 h) ones.
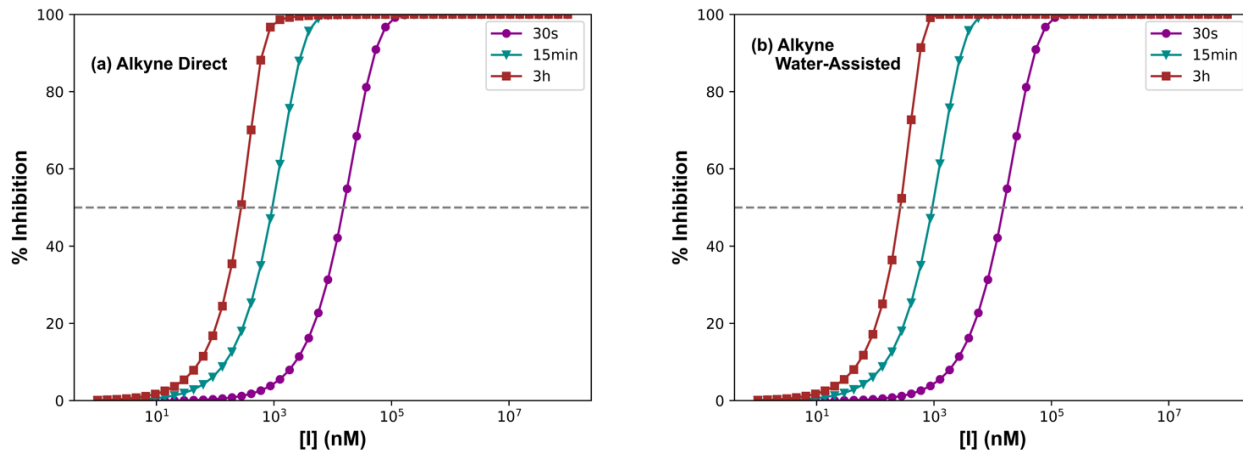
Figure 10. Simulated incubation assay of M^{pro} under different preincubation times in varying concentrations alkyne derivative of Nirmatrelvir for the (a) direct and (b) water assisted. The irreversibility of the reaction with the alkyne warhead is apparent by strong dependence of the IC50 on pre-incubation time.

Conclusions

Our investigation explores the kinetics and thermodynamics of inhibition by two distinct inhibitors, each characterized by different reactive groups: one with a nitrile group and the other with an alkyne group. Using both EVB and PDLD/S-LRA-2000 simulations, we were able to delineate the binding energetics and chemical reactivity for both covalent and non-covalent interactions of these compounds. Our EVB calculations indicate that the water-assisted mechanism is more favorable than the direct mechanism for both inhibitors. The EVB barrier for the nitrile warhead agrees with other QM/MM studies, and while there is no reported activation barrier for the alkyne derivative in the studied system, our EVB barrier falls within the range of other covalent cysteine proteases. The reaction energy for the nitrile is moderately exothermic and reversible, matching other QM/MM studies. In contrast, the reaction energy for the alkyne derivative is highly exothermic and corresponds to an irreversible process, consistent with experimental findings.

Additionally, the insights gained from our kinetic modeling, listed in Table 1, is in close agreement with experimental data and reveal the superior efficacy of the alkyne-modified inhibitor compared to the nitrile over a three-hour period. Overall, this kinetic simulation approach, as demonstrated

for M^{pro} inhibitors, offers a rapid and valuable tool for identifying and assessing potential inhibitor compounds in pharmaceutical development.

Data Availability

Optimized and transition state ab initio structures used for the EVB reference reactions are available at https://github.com/AugustineZAX/covid_IC50/

Acknowledgments

References

(1) Gajjar, N. D.; Dhameliya, T. M.; Shah, G. B. In Search of RdRp and Mpro Inhibitors against SARS CoV-2: Molecular Docking, Molecular Dynamic Simulations and ADMET Analysis. *J. Mol. Struct.* **2021**, *1239*, 130488. https://doi.org/10.1016/j.molstruc.2021.130488.

(2) Gao, X.; Qin, B.; Chen, P.; Zhu, K.; Hou, P.; Wojdyla, J. A.; Wang, M.; Cui, S. Crystal Structure of SARS-CoV-2 Papain-like Protease. *Acta Pharm. Sin. B* **2021**, *11* (1), 237–245. https://doi.org/10.1016/j.apsb.2020.08.014.

(3) Silva, L. R.; da Silva Santos-Júnior, P. F.; de Andrade Brandão, J.; Anderson, L.; Bassi, Ê. J.; Xavier de Araújo-Júnior, J.; Cardoso, S. H.; da Silva-Júnior, E. F. Druggable Targets from Coronaviruses for Designing New Antiviral Drugs. *Bioorg. Med. Chem.* **2020**, *28* (22), 115745. https://doi.org/10.1016/j.bmc.2020.115745.

(4) Dai, W.; Zhang, B.; Jiang, X.-M.; Su, H.; Li, J.; Zhao, Y.; Xie, X.; Jin, Z.; Peng, J.; Liu, F.; Li, C.; Li, Y.; Bai, F.; Wang, H.; Cheng, X.; Cen, X.; Hu, S.; Yang, X.; Wang, J.; Liu, X.; Xiao, G.; Jiang, H.; Rao, Z.; Zhang, L.-K.; Xu, Y.; Yang, H.; Liu, H. Structure-Based Design of Antiviral Drug Candidates Targeting the SARS-CoV-2 Main Protease. *Science* **2020**, *368* (6497), 1331–1335. https://doi.org/10.1126/science.abb4489.

(5) Ullrich, S.; Nitsche, C. The SARS-CoV-2 Main Protease as Drug Target. *Bioorg. Med. Chem. Lett.* **2020**, *30* (17), 127377. https://doi.org/10.1016/j.bmcl.2020.127377.

(6) Mengist, H. M.; Dilnessa, T.; Jin, T. Structural Basis of Potential Inhibitors Targeting SARS-CoV-2 Main Protease. *Front. Chem.* **2021**, *9*, 622898. https://doi.org/doi:10.3389/fchem.2021.622898.

(7) Ziebuhr, J.; Herold, J.; Siddell, S. G. Characterization of a Human Coronavirus (Strain 229E) 3C-like Proteinase Activity. *J. Virol.* **1995**, *69* (7), 4331–4338. https://doi.org/10.1128/jvi.69.7.4331-4338.1995.

(8) Poduri, R.; Joshi, G.; Jagadeesh, G. Drugs Targeting Various Stages of the SARS-CoV-2 Life Cycle: Exploring Promising Drugs for the Treatment of Covid-19. *Cell. Signal.* **2020**, *74*, 109721. https://doi.org/10.1016/j.cellsig.2020.109721.

(9) Gao, K.; Wang, R.; Chen, J.; Tepe, J. J.; Huang, F.; Wei, G.-W. Perspectives on SARS-CoV-2 Main Protease Inhibitors. *J. Med. Chem.* **2021**, *64* (23), 16922–16955. https://doi.org/10.1021/acs.jmedchem.1c00409.

(10) Gimeno, A.; Mestres-Truyol, J.; Ojeda-Montes, M. J.; Macip, G.; Saldivar-Espinoza, B.; Cereto-Massagué, A.; Pujadas, G.; Garcia-Vallvé, S. Prediction of Novel Inhibitors of the Main Protease (M-pro) of SARS-CoV-2 through Consensus Docking and Drug Reposition. *Int. J. Mol. Sci.* **2020**, *21* (11), 3793.

(11) Hasan, M. N.; Ray, M.; Saha, A. Landscape of In Silico Tools for Modeling Covalent Modification of Proteins: A Review on Computational Covalent Drug Discovery. *J. Phys. Chem. B* **2023**, *127* (45), 9663–9684. https://doi.org/10.1021/acs.jpcb.3c04710.

(12) Tuley, A.; Fast, W. The Taxonomy of Covalent Inhibitors. *Biochemistry* **2018**, *57* (24), 3326–3337. https://doi.org/10.1021/acs.biochem.8b00315.

(13) Mestres, J.; Gregori-Puigjané, E.; Valverde, S.; Solé, R. V. The Topology of Drug–Target Interaction Networks: Implicit Dependence on Drug Properties and Target Families. *Mol. Biosyst.* **2009**, *5* (9), 1051–1057. https://doi.org/10.1039/B905821B.

(14) Singh, J.; Petter, R. C.; Baillie, T. A.; Whitty, A. The Resurgence of Covalent Drugs. *Nat. Rev. Drug Discov.* **2011**, *10* (4), 307–317. https://doi.org/10.1038/nrd3410.

(15) Banerjee, R.; Perera, L.; Tillekeratne, L. V. Potential SARS-CoV-2 Main Protease Inhibitors. *Drug Discov. Today* **2021**, *26* (3), 804–816.

(16) Al-Khafaji, K.; AL-DuhaidahawiL, D.; Taskin Tok, T. Using Integrated Computational Approaches to Identify Safe and Rapid Treatment for SARS-CoV-2. *J. Biomol. Struct. Dyn.* **2020**, 1–9. https://doi.org/10.1080/07391102.2020.1764392.

(17) Tung Ngo, S.; Hai Nguyen, T.; Thanh Tung, N.; Khanh Mai, B. Insights into the Binding and Covalent Inhibition Mechanism of PF-07321332 to SARS-CoV-2 M Pro. *RSC Adv.* **2022**, *12* (6), 3729–3737. https://doi.org/10.1039/D1RA08752E.

(18) Paul, A. S.; Islam, R.; Parves, M. R.; Mamun, A. A.; Shahriar, I.; Hossain, M. I.; Hossain, M. N.; Ali, M. A.; Halim, M. A. Cysteine Focused Covalent Inhibitors against the Main Protease of SARS-CoV-2. *J. Biomol. Struct. Dyn.* **2022**, *40* (4), 1639–1658. https://doi.org/10.1080/07391102.2020.1831610.

(19) Mondal, D.; Warshel, A. Exploring the Mechanism of Covalent Inhibition: Simulating the Binding Free Energy of α-Ketoamide Inhibitors of the Main Protease of SARS-CoV-2. *Biochemistry* **2020**, *59* (48), 4601–4608. https://doi.org/10.1021/acs.biochem.0c00782.

(20) Cokley, J. A.; Gidal, B. E.; Keller, J. A.; Vossler, D. G. PaxlovidTM Information From FDA and Guidance for AES Members. *Epilepsy Curr.* **2022**, *22* (3), 201–204. https://doi.org/10.1177/15357597221088415.

(21) Chen, W.; Liang, B.; Wu, X.; Li, L.; Wang, C.; Xing, D. Advances and Challenges in Using Nirmatrelvir and Its Derivatives against SARS-CoV-2 Infection. *J. Pharm. Anal.* **2023**, *13* (3), 255–261. https://doi.org/10.1016/j.jpha.2022.10.005.

(22) Ngo, C.; Fried, W.; Aliyari, S.; Feng, J.; Qin, C.; Zhang, S.; Yang, H.; Shanaa, J.; Feng, P.; Cheng, G.; Chen, X. S.; Zhang, C. Alkyne as a Latent Warhead to Covalently Target SARS-

CoV-2 Main Protease. *J. Med. Chem.* **2023**, *66* (17), 12237–12248. https://doi.org/10.1021/acs.jmedchem.3c00810.

(23) Brewitz, L.; Dumjahn, L.; Zhao, Y.; Owen, C. D.; Laidlaw, S. M.; Malla, T. R.; Nguyen, D.; Lukacik, P.; Salah, E.; Crawshaw, A. D.; Warren, A. J.; Trincao, J.; Strain-Damerell, C.; Carroll, M. W.; Walsh, M. A.; Schofield, C. J. Alkyne Derivatives of SARS-CoV-2 Main Protease Inhibitors Including Nirmatrelvir Inhibit by Reacting Covalently with the Nucleophilic Cysteine. *J. Med. Chem.* **2023**, *66* (4), 2663–2680. https://doi.org/10.1021/acs.jmedchem.2c01627.

(24) Citarella, A.; Dimasi, A.; Moi, D.; Passarella, D.; Scala, A.; Piperno, A.; Micale, N. Recent Advances in SARS-CoV-2 Main Protease Inhibitors: From Nirmatrelvir to Future Perspectives. *Biomolecules* **2023**, *13* (9), 1339. https://doi.org/10.3390/biom13091339.

(25) Zhou, J.; Saha, A.; Huang, Z.; Warshel, A. Fast and Effective Prediction of the Absolute Binding Free Energies of Covalent Inhibitors of SARS-CoV-2 Main Protease and 20S Proteasome. *J. Am. Chem. Soc.* **2022**, *144* (17), 7568–7572. https://doi.org/10.1021/jacs.2c00853.

(26) Tan, B.; Sacco, M.; Tan, H.; Li, K.; Joyce, R.; Zhang, X.; Chen, Y.; Wang, J. Exploring Diverse Reactive Warheads for the Design of SARS-CoV-2 Main Protease Inhibitors. *Eur. J. Med. Chem.* **2023**, *259*, 115667. https://doi.org/10.1016/j.ejmech.2023.115667.

(27) Ramos-Guzmán, C. A.; Ruiz-Pernía, J. J.; Tuñón, I. A Microscopic Description of SARS-CoV-2 Main Protease Inhibition with Michael Acceptors. Strategies for Improving Inhibitor Design. *Chem. Sci.* **2021**, *12* (10), 3489–3496. https://doi.org/10.1039/D0SC04978F.

(28) Ngo, S. T.; Nguyen, T. H.; Tung, N. T.; Mai, B. K. Insights into the Binding and Covalent Inhibition Mechanism of PF-07321332 to SARS-CoV-2 Mpro. *RSC Adv.* **2022**, *12* (6), 3729–3737. https://doi.org/10.1039/D1RA08752E.

(29) Ramos-Guzmán, C. A.; Ruiz-Pernía, J. J.; Tuñón, I. Multiscale Simulations of SARS-CoV-2 3CL Protease Inhibition with Aldehyde Derivatives. Role of Protein and Inhibitor Conformational Changes in the Reaction Mechanism. *ACS Catal.* **2021**, *11* (7), 4157–4168. https://doi.org/10.1021/acscatal.0c05522.

(30) Świderek, K.; Moliner, V. Revealing the Molecular Mechanisms of Proteolysis of SARS-CoV-2 Mpro by QM/MM Computational Methods. *Chem. Sci.* **2020**, *11* (39), 10626–10630. https://doi.org/10.1039/D0SC02823A.

(31) Ramos-Guzmán, C. A.; Ruiz-Pernía, J. J.; Tuñón, I. Unraveling the SARS-CoV-2 Main Protease Mechanism Using Multiscale Methods. *ACS Catal.* **2020**, *10* (21), 12544–12554. https://doi.org/10.1021/acscatal.0c03420.

(32) Owen, D. R.; Allerton, C. M.; Anderson, A. S.; Aschenbrenner, L.; Avery, M.; Berritt, S.; Boras, B.; Cardin, R. D.; Carlo, A.; Coffman, K. J. An Oral SARS-CoV-2 Mpro Inhibitor Clinical Candidate for the Treatment of COVID-19. *Science* **2021**, *374* (6575), 1586–1593.

(33) Van Der Spoel, D.; Lindahl, E.; Hess, B.; Groenhof, G.; Mark, A. E.; Berendsen, H. J. C. GROMACS: Fast, Flexible, and Free. *J. Comput. Chem.* **2005**, *26* (16), 1701–1718. https://doi.org/10.1002/jcc.20291.

(34) Maple, J. R.; Dinur, U.; Hagler, A. T. Derivation of Force Fields for Molecular Mechanics and Dynamics from Ab Initio Energy Surfaces. *Proc. Natl. Acad. Sci.* **1988**, *85* (15), 5350–5354. https://doi.org/10.1073/pnas.85.15.5350.

(35) Frisch, M. ea; Trucks, G. W.; Schlegel, H. B.; Scuseria, G. E.; Robb, M. A.; Cheeseman, J. R.; Scalmani, G.; Barone, V.; Petersson, G. A.; Nakatsuji, H. Gaussian 16, 2016.

(36) Zhao, Y.; Truhlar, D. G. The M06 Suite of Density Functionals for Main Group Thermochemistry, Thermochemical Kinetics, Noncovalent Interactions, Excited States, and Transition Elements: Two New Functionals and Systematic Testing of Four M06-Class Functionals and 12 Other Functionals. *Theor. Chem. Acc.* **2008**, *120* (1), 215–241. https://doi.org/10.1007/s00214-007-0310-x.

(37) Paasche, A.; Schirmeister, T.; Engels, B. Benchmark Study for the Cysteine–Histidine Proton Transfer Reaction in a Protein Environment: Gas Phase, COSMO, QM/MM Approaches. *J. Chem. Theory Comput.* **2013**, *9* (3), 1765–1777. https://doi.org/10.1021/ct301082y.

(38) Marenich, A. V.; Cramer, C. J.; Truhlar, D. G. Performance of SM6, SM8, and SMD on the SAMPL1 Test Set for the Prediction of Small-Molecule Solvation Free Energies. *J. Phys. Chem. B* **2009**, *113* (14), 4538–4543. https://doi.org/10.1021/jp809094y.

(39) Warshel, A.; Weiss, R. M. An Empirical Valence Bond Approach for Comparing Reactions in Solutions and in Enzymes. *J. Am. Chem. Soc.* **1980**, *102* (20), 6218–6226. https://doi.org/10.1021/ja00540a008.

(40) Kamerlin, S. C. L.; Warshel, A. The Empirical Valence Bond Model: Theory and Applications. *WIREs Comput. Mol. Sci.* **2011**, *1* (1), 30–45. https://doi.org/10.1002/wcms.10.

(41) Asadi, M.; Xie, W. J.; Warshel, A. Exploring the Role of Chemical Reactions in the Selectivity of Tyrosine Kinase Inhibitors. *J. Am. Chem. Soc.* **2022**, *144* (36), 16638–16646.

(42) Oanca, G.; Asadi, M.; Saha, A.; Ramachandran, B.; Warshel, A. Exploring the Catalytic Reaction of Cysteine Proteases. *J. Phys. Chem. B* **2020**, *124* (50), 11349–11356. https://doi.org/10.1021/acs.jpcb.0c08192.

(43) Tandarić, T.; Prah, A.; Stare, J.; Mavri, J.; Vianello, R. Hydride Abstraction as the Rate-Limiting Step of the Irreversible Inhibition of Monoamine Oxidase B by Rasagiline and Selegiline: A Computational Empirical Valence Bond Study. *Int. J. Mol. Sci.* **2020**, *21* (17), 6151. https://doi.org/10.3390/ijms21176151.

(44) Prah, A.; Purg, M.; Stare, J.; Vianello, R.; Mavri, J. How Monoamine Oxidase A Decomposes Serotonin: An Empirical Valence Bond Simulation of the Reactive Step. *J. Phys. Chem. B* **2020**, *124* (38), 8259–8265.

(45) Bauer, P.; Barrozo, A.; Purg, M.; Amrein, B. A.; Esguerra, M.; Wilson, P. B.; Major, D. T.; Åqvist, J.; Kamerlin, S. C. L. Q6: A Comprehensive Toolkit for Empirical Valence Bond and Related Free Energy Calculations. *SoftwareX* **2018**, *7*, 388–395. https://doi.org/10.1016/j.softx.2017.12.001.

(46) Mark, P.; Nilsson, L. Structure and Dynamics of the TIP3P, SPC, and SPC/E Water Models at 298 K. *J. Phys. Chem. A* **2001**, *105* (43), 9954–9960. https://doi.org/10.1021/jp003020w.

(47) King, G.; Warshel, A. A Surface Constrained All-atom Solvent Model for Effective Simulations of Polar Solutions. *J. Chem. Phys.* **1989**, *91* (6), 3647–3661. https://doi.org/10.1063/1.456845.

(48) Lee, F. S.; Warshel, A. A Local Reaction Field Method for Fast Evaluation of Long-range Electrostatic Interactions in Molecular Simulations. *J. Chem. Phys.* **1992**, *97* (5), 3100–3107. https://doi.org/10.1063/1.462997.

(49) Warshel, A. *Computer Modeling of Chemical Reactions in Enzymes and Solutions*; Wiley: New York, 1991.

(50) Lee, F. S.; Chu, Z. T.; Warshel, A. Microscopic and Semimicroscopic Calculations of Electrostatic Energies in Proteins by the POLARIS and ENZYMIX Programs. *J. Comput. Chem.* **1993**, *14* (2), 161–185. https://doi.org/10.1002/jcc.540140205.

(51) Singh, N.; Warshel, A. Absolute Binding Free Energy Calculations: On the Accuracy of Computational Scoring of Protein–Ligand Interactions. *Proteins Struct. Funct. Bioinforma.* **2010**, *78* (7), 1705–1723. https://doi.org/10.1002/prot.22687.

(52) Sham, Y. Y.; Chu, Z. T.; Tao, H.; Warshel, A. Examining methods for calculations of binding free energies: LRA, LIE, PDLD-LRA, and PDLD/S-LRA calculations of ligands binding to an HIV protease. *Proteins Struct. Funct. Bioinforma.* **2000**, *39* (4), 393–407. https://doi.org/10.1002/(SICI)1097-0134(20000601)39:4<393::AID-PROT120>3.0.CO;2-H.

(53) Nandi, A.; Zhang, A.; Arad, E.; Jelinek, R.; Warshel, A. Assessing the Catalytic Role of Native Glucagon Amyloid Fibrils. *ACS Catal.* **2024**, *14* (7), 4656–4664. https://doi.org/10.1021/acscatal.4c00452.

(54) Warshel, A.; Chu, Z. T.; Villa, J.; Strajbl, M.; Schutz, C.; Shurki, A.; Vicatos, S.; Plotnikov, N.; Schopf, P. *Molaris-Xg, Version 9.15*; University of Southern California: Los Angeles, 2012.

(55) Lee, F. S.; Chu, Z.-T.; Bolger, M. B.; Warshel, A. Calculations of Antibody-Antigen Interactions: Microscopic and Semi-Microscopic Evaluation of the Free Energies of Binding of Phosphorylcholine Analogs to McPC603. *Protein Eng. Des. Sel.* **1992**, *5* (3), 215–228. https://doi.org/10.1093/protein/5.3.215.

(56) Muegge, I.; Tao, H.; Warshel, A. A Fast Estimate of Electrostatic Group Contributions to the Free Energy of Protein-Inhibitor Binding. *Protein Eng. Des. Sel.* **1997**, *10* (12), 1363–1372. https://doi.org/10.1093/protein/10.12.1363.

(57) Warshel, A.; Sharma, P. K.; Kato, M.; Parson, W. W. Modeling Electrostatic Effects in Proteins. *Biochim. Biophys. Acta BBA - Proteins Proteomics* **2006**, *1764* (11), 1647–1676. https://doi.org/10.1016/j.bbapap.2006.08.007.

(58) Schutz, C. N.; Warshel, A. What Are the Dielectric "Constants" of Proteins and How to Validate Electrostatic Models? *Proteins Struct. Funct. Bioinforma.* **2001**, *44* (4), 400–417. https://doi.org/10.1002/prot.1106.

(59) Štrajbl, M.; Florián, J.; Warshel, A. Ab Initio Evaluation of the Free Energy Surfaces for the General Base/Acid Catalyzed Thiolysis of Formamide and the Hydrolysis of Methyl Thiolformate: A Reference Solution Reaction for Studies of Cysteine Proteases. *J. Phys. Chem. B* **2001**, *105* (19), 4471–4484. https://doi.org/10.1021/jp010279l.

(60) Ramos-Guzmán, C. A.; Ruiz-Pernía, J. J.; Tuñón, I. Computational Simulations on the Binding and Reactivity of a Nitrile Inhibitor of the SARS-CoV-2 Main Protease. *Chem. Commun.* **2021**, *57* (72), 9096–9099. https://doi.org/10.1039/D1CC03953A.

(61) Arafet, K.; Ferrer, S.; Moliner, V. Computational Study of the Catalytic Mechanism of the Cruzain Cysteine Protease. *ACS Catal.* **2017**, *7* (2), 1207–1215. https://doi.org/10.1021/acscatal.6b03096.

(62) Kozuch, S.; Shaik, S. How to Conceptualize Catalytic Cycles? The Energetic Span Model. *Acc. Chem. Res.* **2011**, *44* (2), 101–110. https://doi.org/10.1021/ar1000956.

(63) Chakrabarty, S.; Warshel, A. Capturing the Energetics of Water Insertion in Biological Systems: The Water Flooding Approach. *Proteins Struct. Funct. Bioinforma.* **2013**, *81* (1), 93–106. https://doi.org/10.1002/prot.24165.

(64) Dos Santos, A. M.; Oliveira, A. R. S.; da Costa, C. H. S.; Kenny, P. W.; Montanari, C. A.; Varela, J. de J. G. J.; Lameira, J. Assessment of Reversibility for Covalent Cysteine Protease Inhibitors Using Quantum Mechanics/Molecular Mechanics Free Energy Surfaces. *J. Chem. Inf. Model.* **2022**, *62* (17), 4083–4094. https://doi.org/10.1021/acs.jcim.2c00466.

(65) Mons, E.; Jansen, I. D. C.; Loboda, J.; van Doodewaerd, B. R.; Hermans, J.; Verdoes, M.; van Boeckel, C. A. A.; van Veelen, P. A.; Turk, B.; Turk, D.; Ovaa, H. The Alkyne Moiety as a Latent Electrophile in Irreversible Covalent Small Molecule Inhibitors of Cathepsin K. *J. Am. Chem. Soc.* **2019**, *141* (8), 3507–3514. https://doi.org/10.1021/jacs.8b11027.

Table of Contents

Nitrile Warhead

"Reversible"

Alkyne Warhead

"Irreversible"

Proton transfer ——— Proton transfer-nucleophilic attack